Nanoscale

Accepted Manuscript

This article can be cited before page numbers have been issued, to do this please use: C. V. Chinnappa, K. R. Ag, T. H. T. Nguyen, Z. Zarkua, I. Abbas, T. H. Hoang, P. Lievens, D. Grandjean, S. W. Verbruggen and E. Janssens, *Nanoscale*, 2024, DOI: 10.1039/D4NR03219E.

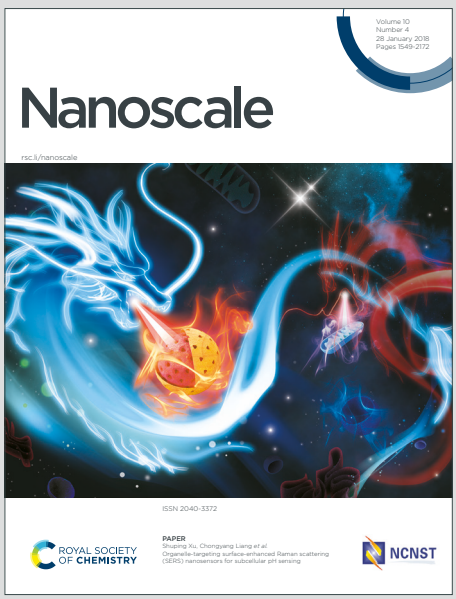

ROYAL SOCIETY OF CHEMISTRY

rsc.li/nanoscale

View Article Online
DOI: 10.1039/D4NR03219E

ARTICLE

AuCu bimetallic nanocluster-modified titania nanotubes for photoelectrochemical water splitting: composition-dependent atomic arrangement and activity

aReceived 00th January 20xx,
Accepted 00th January 20xx

DOI: 10.1039/x0xx00000x

Vana Chinnappa Chinnabathini[a,b], Karthick Raj Ag[b], Thi Hong Trang Nguyen[a], Zviadi Zarkua[a], Imran Abbas[a], Thi Hang Hoang[a], Peter Lievens[a], Didier Grandjean[a]*, Sammy W. Verbruggen[b]*, Ewald Janssens[a]*

The photoelectrochemical (PEC) water splitting reaction on bimetallic Au_xCu_{1-x} (x = 1, 0.75, 0.5, 0.25 and 0) nanocluster-decorated TiO_2 nanotubes (TNTs) photoanode was investigated using a solar simulator. A strong enhancement in the anodic photocurrent relative to pristine TNTs was found with a clear composition-dependent PEC activity, increasing with Cu content and peaking at $Au_{0.25}Cu_{0.75}$. Electron microscopy and X-ray Absorption Fine Structure measured at both Au and Cu edges identified a clear composition-dependent atomic arrangement of the spherical nanoclusters on anatase TNTs, resulting mostly from a time-dependent restructuring of the original metallic nanoalloys in the ambient. Upon time, Cu segregates from the alloy to form a surface oxide layer surrounding a pure gold metallic core in the gold-rich nanoclusters (x = 0.75 and 0.50) or an face centered tetragonal(fct)-intermetallic $Au_{0.5}Cu_{0.5}$ nanoalloy in copper-rich (x = 0.25) particles. In the pure Cu nanoclusters, a metallic Cu core is stabilized by surrounding Cu_2O and CuO. The enhanced PEC activity is attributed to a synergy between Au and Cu that upon segregation produce bifunctional catalytic sites consisting of metallic Au/AuCu alloy and copper oxide at the surface of the nanoclusters. The photoactivity under solar light illumination is boosted by the plasmonic response of the metal. The ordered structure of the ftc-AuCu alloy present in the most active $Au_{0.25}Cu_{0.75}$ may explain its higher stability and photocatalytic performance. Hence, this work provides insight in the relationship between the atomic-level structure of Au_xCu_{1-x} nanoalloys on TNTs and their PEC activity.

1. Introduction

The n-type semiconductor titanium dioxide is known for its good stability, high resistance to corrosion, non-toxicity, bio-compatibility, and low production cost. TiO_2 nanostructures, including nanoparticles,[1] nanowires,[2] nanorods,[3] nanotubes,[4] and nanopores[5] are intensively studied, particularly for photocatalysis. Anodic oxidation of a metallic titanium foil allows for straightforward and efficient synthesis of highly ordered titania nanotubes (TNTs), whose length and diameter can be conveniently tuned by the applied voltage, anodizing time, annealing temperature, and the composition of the electrolyte.[6-9] Since the pioneering work of Zwilling et. al.[10] on the anodic oxidation of titanium into highly ordered titania nanotubes, the morphology of TNTs and their potential applications in catalysis has been studied extensively. Self-assembled TNT arrays possess exceptional structural, electrical, thermal and optical properties.[11-16] They have a highly ordered structure, high mechanical and chemical stability, good corrosion resistance, high specific surface area,[17,18] enhanced charge transfer, and a large number of active sites.[19,20] Those properties make TNTs useful for applications in photocatalysis,[21] solar cells, environmental purification, water photolysis, gas sensing, and bio-medicine.[22,23] By diminishing dimensions to the nanoscale, the specific surface area increases, while the modified electronic structure of the TNTs diminishes the electron-hole recombination rate. The large effective surface area in direct contact with the electrolyte enables diffusive transport of photogenerated holes to the oxidizable species in the electrolyte of photoelectrochemical (PEC) cells. The effects of annealing temperature, crystallinity, wall thickness, tube length and diameter of the TNTs on the PEC activity has been discussed in several reviews.[24-26]

TiO_2 has suitable band-edge positions for electrochemical water splitting with the bottom of the conduction band being more negative than the H_2/H_2O redox potential (0 V) and the top of the valence band being more positive than the H_2O/O_2 redox potential (–1.23 V).[27,28] A drawback is its relatively large bandgap (≈3.2 eV in the anatase phase), requiring UV light for efficient operation. Various modifications, particularly the incorporation of metal nanoparticles, have been employed to enable visible light driven processes. Cu, Ag, and Au nanoparticles possess a strong ability to absorb solar photons due to the localized surface plasmon resonance (LSPR) effect,[29] and can transfer energetic electrons formed in the LSPR process to a nearby semiconductor.[30] LSPR-induced near-field enhancement at the surface of the metallic nanostructures can contribute to the generation of electron-hole pairs. It has been well established that metal nanoparticles on the surface of TiO_2 can act as traps for photo-induced electrons, preventing fast recombination of charge carriers,[31,32] and thus enhancing the PEC activity of TNT electrodes.

[a] Quantum Solid-State Physics, Department of Physics and Astronomy, KU Leuven, Belgium. ewald.janssens@kuleuven.be; didier.grandjean@kuleuven.be;
[b] Sustainable Energy, Air & Water Technology (DuEL), University of Antwerp, Belgium. sammy.verbruggen@uantwerpen.be

Electronic Supplementary Information (ESI) available: additional sample characterisation data and assessment of the potential current generated by the oxidation of copper. See DOI: 10.1039/x0xx00000x

Several examples of improved photocurrents in TNTs decorated with monometallic Cu, Ag, or Au nanoparticles can be found in literature.[33-37] For instance, photocurrent densities of about 90 μA/cm^2 and 80 μA/cm^2 were recorded under 350 nm irradiation and an applied voltage of 1 V versus the saturated calomel electrode, 1 V_{SCE} for TNTs modified with Cu and Ag, respectively.[38] The modification of TNTs with plasmonic bimetallic nanoparticles combines the LSPR effect with properties from both metals, [39-42] and provides highly active metal–support interfaces suitable for PEC reactions.[41] For example, TNTs modified with atomically precise AuCu alloy nanoparticles were found to exhibit an improved photocurrent under visible light irradiation in comparison with a blank TNT substrate.[43] Also TNTs modified with AuCu nanoparticles that are thermally treated in argon exhibited a higher photocurrent (64 μA/cm^2 at −0.2 V) under UV−Vis light as a pristine TNT electrode (32 μA/cm^2).[44]

The modification of TNTs with bimetallic AuCu nanoalloys takes advantage of a synergy between the highly stable and plasmonic active noble metal Au and the less stable but also less expensive and more electrocatalytically active metal Cu. Utilising this promising combination requires good understanding of the effect of composition on the structural arrangement. Such information is, to the best of our knowledge, lacking.

The aim of the current study is to modify TNTs with well-defined gas-phase prepared AuCu particles with nanometer sizes, hereafter called nanoclusters (NCs) and explore the composition-dependent relationship between their PEC performance for water splitting and the atomic NC arrangement. For this purpose, we have synthesized and deposited small-sized (< 5 nm) AuCu NCs at a low metal loading (about 1 μg/cm^2) on TNTs with a good control over the composition and coverage and tested their PEC water splitting performance. The AuCu-modified TNTs photoanodes exhibit an excellent photostability and high composition-dependent photoactivity in the visible range of the solar spectrum. Alloy NCs with different compositions were synthesized through the physical cluster beam deposition (CBD) process[48] that produces ligand-free, size- and composition-tuneable NCs with high degree of purity and uniform coverage.

2. Results

2.1. Structural characterization

The gas-phase size distribution of Au_xCu_{1-x} clusters, produced in a laser ablation source by ablating alloy targets with x = 1, 0.75, 0.5, 0.25, and 0 followed by inert gas condensation, is recorded using in situ time-of-flight mass spectrometry. Assuming a spherical shape and bulk density for all NC compositions, the diameter distribution of the clusters prior to deposition has a maximum around 2 nm (see supplementary information, Figure S1). Because the detection efficiency of larger clusters by the microchannel plate detector is lower, the real average size of the clusters in the gas phase is likely larger. The loading of the NCs is determined by the deposition time and the mass flux measured before and after cluster deposition using a quartz crystal microbalance (QCM). Typical fluxes are 0.062 μg /cm^2/minute. A total mass loading of 1.1 μg /cm^2 has been deposited for the samples discussed in this work, which can also be expressed in an equivalent height of a hypothetical thin film of 4 atomic monolayers (ML, *i.e.* a thickness equivalent to a film of 0.25 nm).

X-ray diffraction (XRD) patterns of the annealed TNTs modified by AuCu NCs measured after PEC measurements are provided as supplementary information, Figure S2**.** The characteristic diffraction peaks of TiO_2 anatase are observed as well as the underlying metallic titanium substrate of the electrode on which the TNTs were grown. In line with previous studies on TNTs modified with small metal clusters,[45,46] no diffraction peaks of the deposited clusters could be detected, likely due to the low loading. The intense (004) diffraction peak observed for all samples indicates a preferred [001]-oriented anatase phase in TNT with the (004) lattice plane perpendicular to their axis. The variation in the relative intensity of the anatase (004) and (101) peaks reflect variations of the orientation of the TNTs relative to the Ti substrate.[47]

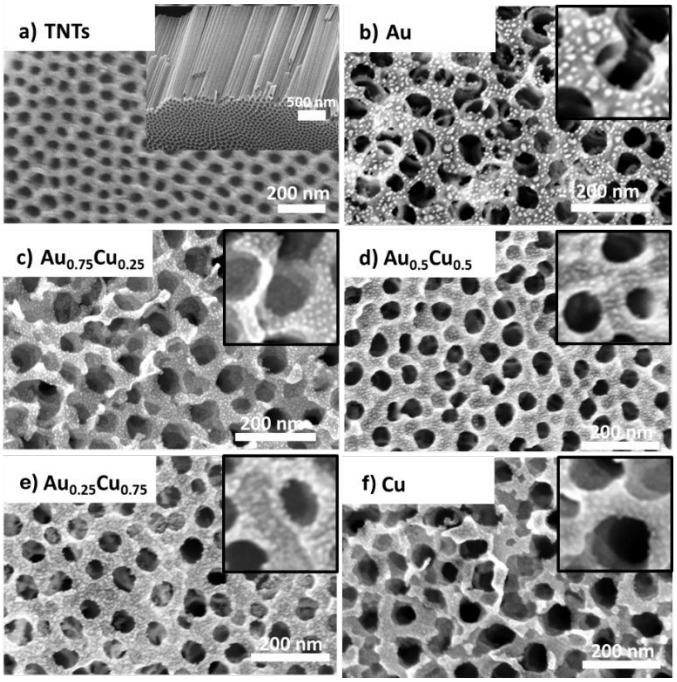

Figure 1. SEM images of a) top-view of pristine TNTs with a cross-sectional image in the inset. TNTs covered with 4 ML of b) Au, c) $Au_{0.75}Cu_{0.25}$, d) $Au_{0.5}Cu_{0.5}$, e) $Au_{0.25}Cu_{0.75}$, and f) Cu NCs. The NCs are visible in the insets that zoom in on a 140 × 140 nm² area.

Figure 1 shows top-view and cross-sectional scanning electron microscopy (SEM) images of the pristine and NC decorated TNTs. The TNTs have an ordered nano-morphology with an average tube diameter of *ca*. 60 nm, a wall thickness of *ca*. 15 nm, or an inner diameter of *ca*. 30 nm, and a tube length of ca. 2.5 μm (Figure 1a). The metal decorated samples present randomly distributed clusters (i.e. the small bright dots in Figures 1) on the top surface and the inner walls of the TNTs. Although no apparent sign of cluster agglomeration is observed, it cannot be excluded as the resolution of the SEM (0.8 nm @ 30 keV) is of the order of the size of the clusters. Pure gold NCs appear brighter and slightly larger (Figure 1b).

More information about the morphology, size, structure and composition of alloy NCs is obtained by high-angle annular dark-field (HAADF) scanning transmission electron microscopy (STEM) studies. Figure 2a presents an electron microscopy image of a sample with a 0.67 ML loading of $Au_{0.25}Cu_{0.75}$ NCs deposited on a carbon TEM grid. The NCs are uniformly dispersed and have an average diameter of 3.5 ± 0.5 nm. Energy dispersive x-ray (EDX) mapping of the $Au_{0.25}Cu_{0.75}$ NCs shows that many clusters have an alloyed surface (pale yellow) covered by a significant amount of pure copper patches consisting likely of Cu oxide and a limited amount of pure gold ones (Figure 2b). EDX elemental mapping over a larger area indicates that the composition of an ensemble of deposited $Au_{0.25}Cu_{0.75}$ NCs is 22.7% Au and 77.3% Cu, in line with the composition of the ablated

alloy target (see supplementary information, Figure S3).[48,49] We assume the same holds for the average compositions of the other AuCu NCs based on our observations for NCs with different Au/Ag ratios that were produced using the same cluster source.[40,59]

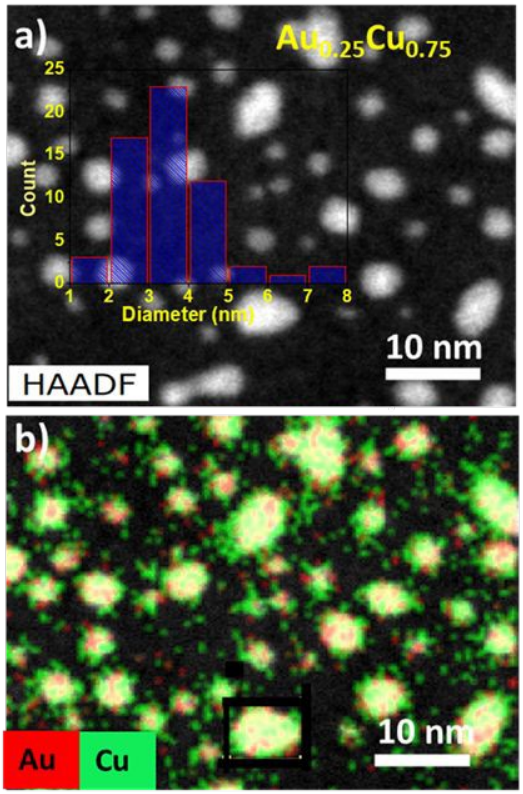

Figure 2. (a) HAADF-STEM with size distribution of NCs obtained from image analysis and b) EDX elemental mapping Cu (green), Au (red) of the $Au_{0.25}Cu_{0.75}$ NCs.

The slightly larger size distribution observed with TEM compared to the mean diameters obtained by mass spectrometry in the gas-phase may be attributed to the above mentioned less efficient detection of the larger mass clusters by the microchannel plate detector of the mass spectrometer (particularly for the used acceleration voltage < 3 kV).[50] Additionally, flattening of the clusters due to cluster-support interaction after deposition and some cluster agglomeration may also contribute to the larger observed sizes.

More information on the composition and the oxidation states of gold and copper in the Au_xCu_{1-x}/TiO_2 (x = 0.75, 0.50, and 0.25) samples was obtained by X-Ray Photoelectron Spectroscopy (XPS). The XPS survey spectrum (see supplementary information, Figure S4) shows that O, C, Ti, Au and Cu are present on the surface of all samples. The O 1s contribution is representative for the oxidation of the Cu phase, while the peak intensity of C 1s is relatively consistent for all the samples despite their varying compositions. Au $4f_{7/2}$ and $4f_{5/2}$ contributions are observed at binding energies of around 84 eV and 88 eV, while the Au $4d_{5/2}$ and $4d_{3/2}$ core levels locate around 334 eV and 355 eV. Upon increasing the Cu concentration, a blue shift of the Au $4d_{5/2}$ binding energy to 337.8 eV is observed both in $Au_{0.5}Cu_{0.5}$ and $Au_{0.25}Cu_{0.75}$, while it is 335.8 eV in $Au_{0.75}Cu_{0.25}$ (Figure 3a). The observation that the Au $4d_{5/2}$ binding energy in $Au_{0.75}Cu_{0.25}$ is close to that of bulk gold hints at the presence of pure gold in these NCs. The large blue shift found for $Au_{0.5}Cu_{0.5}$ and $Au_{0.25}Cu_{0.75}$ implies a depletion of the Au d-states, which is indicative for the formation of an alloy, as reported for a variety of Au-based alloys, including AuCu.[51-55]

The detailed atomic structural arrangement in the Au_xCu_{1-x} NCs was further characterized by X-ray absorption spectroscopy carried out at the Cu and Au edges before performing the PEC studies. X-Ray Absorption Near Edge structure (XANES) spectra measured at the Au L_3-edge of the alloy samples are presented in Figure 3b.

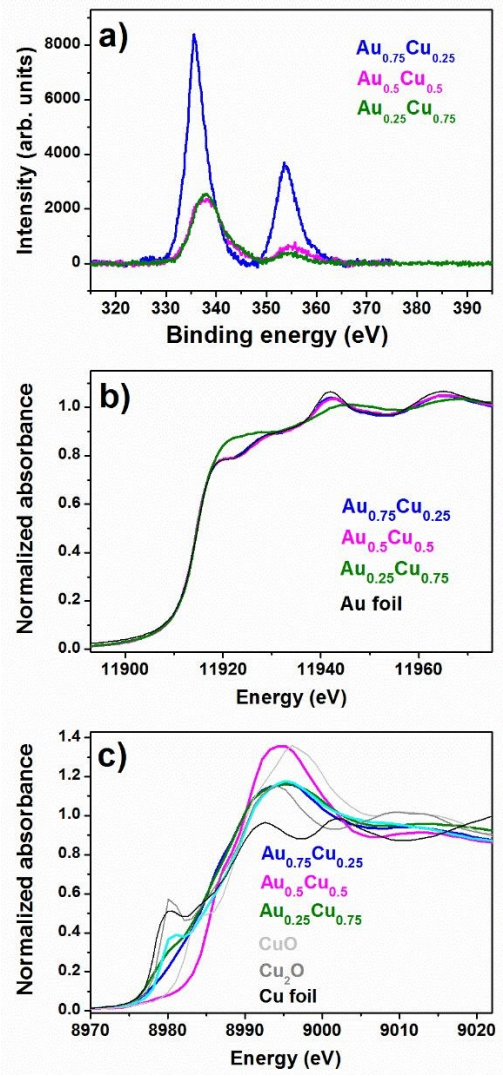

Figure 3. a) XPS core level Au-4d spectra recorded for Au_xCu_{1-x}/TNT (x = 0.75, 0.5, and 0.25). XANES spectra of b) Au-L_3 edge and c) Cu K-edge.

The XANES profiles of $Au_{0.75}Cu_{0.25}$ and $Au_{0.5}Cu_{0.5}$ are similar to that of the Au foil reference, indicating that mostly pure gold is present in these two alloy samples. On the other hand, in $Au_{0.25}Cu_{0.75}$ one can see a sharp increase of the absorption near the edge, which is called the white line intensity and reflects for the Au L_3-edge the unoccupied density of d states above the Fermi level. This increase indicates a clear charge loss from the Au d states, which is likely due to charge transfer from Au to Cu, occurring upon the formation of an AuCu alloy.[56] Similar observations were made for AuAg nanoalloys produced in the same source.[48] This is supported by the observation of an increase of the Au 4d binding energy in the XPS data. Unoccupied d states above the Fermi level in Cu, Ag, and Au alloys are generally compensated by a gain of mainly s-p charge from Cu.[53,57,58] In $Au_{0.5}Cu_{0.5}$ a discrepancy is observed between the XPS

measured a few days after the synthesis, showing the formation of an alloy, and the XANES measured a few months later, pointing out an Au rich phase. This could be due to a lower stability of the $Au_{0.5}Cu_{0.5}$ NCs where Cu tends to segregate from the alloy in the ambient. All alloy Au_xCu_{1-x}/TiO_2 samples contain a significant amount of copper oxide as shown by the systematic blue shift of the Cu K-edge position, accompanied by the marked increase in the white line intensity (Figure 3c). $Au_{0.5}Cu_{0.5}$ contains a large amount of CuO, while a complex mixture of metallic Cu, Cu_2O and CuO is found in $Au_{0.75}Cu_{0.25}$ and $Au_{0.25}Cu_{0.75}$.

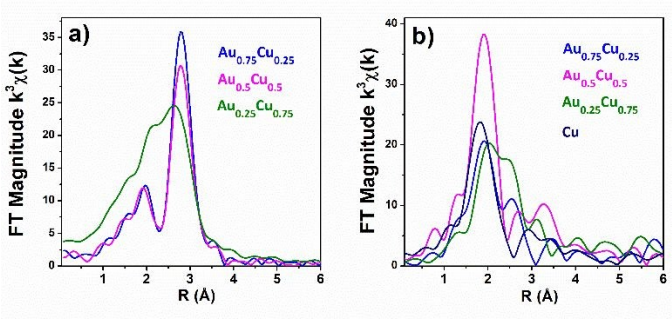

Figure 4. Phase-corrected Fourier-transformed a) Au L_3 -edge and b) Cu K-edge XAFS spectra of the AuCu NCs/TNT samples.

Extended X-ray Absorption Fine Structure (EXAFS) allows for a precise detection of the alloyed structure in nanostructured bimetallic AuCu systems.[59,60] The Fourier transformed spectra of Au L_3-edge k^3-weighted EXAFS of $Au_{0.75}Cu_{0.25}$ and $Au_{0.5}Cu_{0.5}$ are similar, while that of $Au_{0.25}Cu_{0.75}$ is distinct (Figure 4a). Detailed fitting of the Au L_3-edge EXAFS data was carried out with a 2-shell structure model based on Au–Au and Au-Cu (see supplementary information Figure S7 and Table S1). No Au–O interactions could be detected, indicating the fully metallic state of Au in the clusters. Au-Au atomic bond distances sharply decrease with increasing Cu content from 2.85 Å in gold-rich $Au_{0.75}Cu_{0.25}$, over 2.84 Å in $Au_{0.5}Cu_{0.5}$, to 2.81 Å in copper-rich $Au_{0.25}Cu_{0.75}$. The first two distances are similar to the contracted distances of 2.85 Å (relative to the bulk value of 2.88 Å[61,62]) measured in pure gold clusters,[63] indicating the presence of nearly pure gold phase in these materials in line with the XANES analysis. The small Au-Cu contribution of 0.6 Cu with bond distance of 2.64 Å in $Au_{0.75}Cu_{0.25}$ implies the presence of a small fraction of a copper-rich alloy in this sample. No Au-Cu contribution could be detected in $Au_{0.5}Cu_{0.5}$, while in $Au_{0.25}Cu_{0.75}$ the Au-Cu contribution (5.5 Cu at 2.66 Å) is comparable to the Au-Au signal, indicative for the formation of an ordered intermetallic face centered tetragonal (fct) AuCu alloy. Also, this prediction is consistent with the XANES profile in Figure 3b.

Fourier transforms of Cu K-edge k^3-weighted EXAFS in Figure 4b show distinct profiles for the different samples, but they have a common peak below 2 Å indicative for the presence of a significant fraction of oxides. EXAFS fitting results at the copper edge of bimetallic AuCu and pure Cu clusters (see supplementary information Figure S8 and Table S2) show that the first coordination shell consists of 2.27 O at 1.93 Å in pure Cu, 1.8 O at 1.93 Å in $Au_{0.75}Cu_{0.25}$, 2.9 O at 1.96 Å in $Au_{0.5}Cu_{0.5}$, and 1.93 O at 1.94 Å in $Au_{0.25}Cu_{0.75}$. As Cu is four-fold coordinated to O at 1.96 Å in CuO and two-fold coordinated at 1.85 Å, the fraction of copper oxide in each sample, either CuO or Cu_2O, can be calculated using a simple combination of both coordination numbers and bond distances. Fractions of *ca*. 15 % (7% of Cu_2O and 8% of CuO), 36% of CuO_x, 42% (13% of Cu_2O and 29% of CuO), and 73% (40% of Cu_2O and 33% of CuO) are obtained for $Au_{0.75}Cu_{0.25}$, $Au_{0.5}Cu_{0.5}$, $Au_{0.25}Cu_{0.75}$, and Cu, respectively. Cu-Au contributions of 1.9 Au at 2.63 Å and 4.56 Au at 2.63 Å could be respectively fitted in $Au_{0.75}Cu_{0.25}$ and $Au_{0.25}Cu_{0.75}$ confirming the presence of AuCu alloys in these materials. Cu-Cu contributions are 2.3 Cu at 2.57 Å (bulk metal value is 2.56 Å), 1.5 Cu at 2.52 Å, 1.16 Cu at 2.53 Å and 1.37 Cu at 2.56 Å in $Au_{0.75}Cu_{0.25}$, $Au_{0.5}Cu_{0.5}$, and $Au_{0.25}Cu_{0.75}$ and pure Cu, respectively.

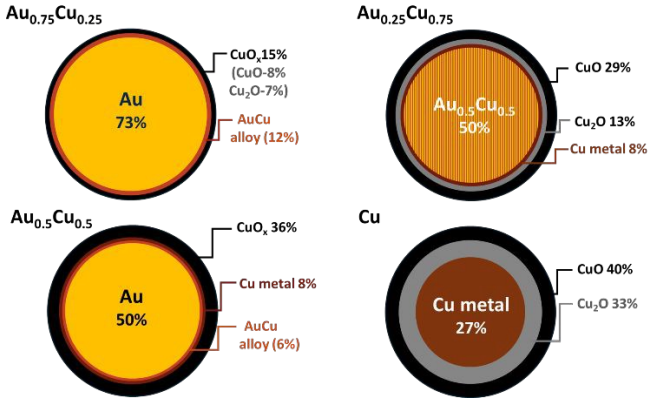

Figure 5. Schematic representations of predicted NC cross-section as implied from the XAFS data analysis.

Based on the obtained bond lengths, coordination numbers, and the fractions of copper oxide, structural models for the different NCs could be proposed (see Figure 5). All the Cu containing samples present a significant fraction of copper oxide at the outer shell resulting from the segregation and oxidation of Cu at the surface of the NCs. Pure Cu clusters have the highest fraction of oxides of ca. 73%, as Cu is prone to oxidation in ambient conditions, while $Au_{0.75}Cu_{0.25}$ has the highest metallic fraction (85%), surrounded by 15% of copper oxide due to the protecting effect of gold. $Au_{0.5}Cu_{0.5}$ has *ca.* 50% of Au at the core covered by 14% of AuCu alloy and pure metallic Cu followed by 36% of copper oxide. Interestingly in $Au_{0.25}Cu_{0.75}$ *ca.* 50% of intermetallic $Au_{0.5}Cu_{0.5}$ alloy forms at the core covered by 8% Cu metal and 42% copper oxide on the surface. These results highlight the very distinct and complex restructuring processes occurring in the initially alloyed Au_xCu_{1-x} NCs as a function of time and composition when they are exposed to ambient conditions. We generally observe the formation of a copper oxide shell consisting of CuO species at the surface and a Cu_2O layer between the CuO and the metallic core. The segregation of copper to the surface results in the formation of a mostly pure Au core in the gold-rich samples. However, the high stability of the AuCu intermetallic alloy combined with the thick Cu oxide passivation layer stop the Cu segregation in copper-rich nanoalloys when the 1:1 stoichiometry is reached. In $Au_{0.5}Cu_{0.5}$ the same AuCu intermetallic alloy is likely formed originally over the whole cluster and remains stable in air for a few days as demonstrated by the XPS. However, on longer times the stability of the intermetallic alloy is not sufficient to prevent segregation. Oxidation of copper and destabilisation of the intermetallic structure by departing from the 1:1 stoichiometry and a full copper segregation is observed after a few months. This detailed structural characterisation highlights the very distinctive atomic arrangement occurring in the bimetallic NCs as a function of their composition leading to different surface and cores (pure metal, random and/or ordered intermetallic alloys) that are expected to affect significantly their stability and photocatalytic activity. Although Cu oxide is located at the surface of the clusters, it is not forming a complete layer but rather grains on the surface of the metallic alloy as shown by the EDX-STEM images of the $Au_{0.25}Cu_{0.75}$ clusters in Figure 2. This structural configuration likely results in the

formation of a dual structure with both phases accessible for the catalytic reaction.

As photocatalysis is a complex process, involving plasmonic, catalytic, and charge transfer and separation processes between the TNTs and the nanoalloys, the nature and size of the metallic core of the NCs as well as the nature of their surface are expected to be important for the PEC activity and stability.

2.2 Optical characterization

Figure 6a presents the UV-Vis absorption spectra of pristine and Au_xCu_{1-x} (x = 1, 0.75, 0.5, 0.25 and 0) NC-modified TNTs with 4 ML loading. All samples exhibit a photoresponse below 400 nm, which can be attributed to the intrinsic band gap of TiO_2. This indicates that surface modification of the TNTs with NCs does not affect the inherent absorption of TiO_2 in the ultraviolet range. At wavelengths above 400 nm, the absorption significantly changes by the presence of the NCs. All cluster-modified samples have a higher absorption in the visible range and the absorption maximum shifts to longer wavelengths compared to bare TNTs. The LSPR intensity of Cu NCs is damped, likely due to their oxidation in air to Cu_2O and CuO.[64,65]

Although the photoresponse of TiO_2 is usually exclusively in the ultraviolet region with wavelengths below 390 nm, the pure TNTs studied in this work show a broad absorption band in the visible range, be it less intense than the one after Au_xCu_{1-x} NC deposition. This band can result from light scattering caused by pores and cracks in the nanotubes and/or to oxygen vacancies and Ti^{3+} states positioned below the TiO_2 conduction band.[66,67] Finally, the absorption in the visible range may also stem from absorption in the underlying Ti metal related to interband d-d transitions.[68] However, incident photon-to-electron conversion efficiency (IPCE) measurements show that no significant photocurrent is generated when the pristine TNTs are illuminated with purely visible light.[69] Therefore, the absorption above 500 nm in all the samples could arise not only from the distinctive highly periodically porous structure of TNTs, as previously reported[70,71] but also from the LSPR of NCs active in the visible range.

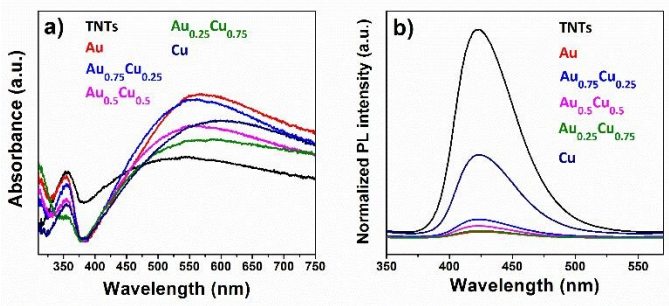

Figure 6. a) UV-Vis absorbance spectra (300 - 750 nm) of pristine and Au_xCu_{1-x} (x= 1, 0.75, 0.5, 0.25 and 0) cluster-modified TNTs with a loading of 4 ML. The absorbance spectra are baseline corrected but not normalized. b) Photoluminescence spectra at an excitation wavelength of 310 nm, normalized for the optical absorbance at the excitation wavelength.

The photoluminescence (PL) spectra of Au_xCu_{1-x} (x = 1, 0.75, 0.5, 0.25 and 0) NC-decorated TNTs samples, measured at an excitation of 310 nm, are presented in Figure 6b. Since the radiative recombination of photogenerated carriers and holes takes place close to the surface,[72] PL spectra are sensitive to molecular adsorption and chemical reactions at the surface of the semiconductor. The PL intensity quantifies the recombination efficiency of photogenerated charges, which is one of the most important limiting factors for photocatalytic efficiency. The intense PL in the visible range observed for pristine TNTs indicates a rapid recombination. All NC-modified samples exhibited a much lower PL intensity than the bare TNTs, which suggests a significant reduction of the electron-hole recombination.[68,73,74] The lowest PL emission is seen for pure Au NCs on TNT, followed by different alloys $Au_{0.25}Cu_{0.75}$ < $Au_{0.5}Cu_{0.5}$ < $Au_{0.75}Cu_{0.25}$, while the pure Cu NCs reduce the PL of the TNTs the least. When the NCs are deposited on TNTs, migration of excited electrons from the semiconductor to the metal occurs until the two Fermi levels are aligned and a Schottky barrier forms at the Au_xCu_{1-x}/TNTs interface, which serves as an efficient electron trap and prevents electron-hole recombination.[75] Those trapped electrons are available for redox reactions.

2.3. Photoelectrochemical performances

The photoelectrochemical activity of the pristine and Au_xCu_{1-x} (x = 1, 0.75 ,0.5, 0.25 and 0) NC-modified TNT electrodes was tested using a standard three electrode PEC cell in 0.5 M Na_2SO_4 electrolyte (at pH 7.2) under AM 1.5G illumination (100 mW/cm^2). When the semiconductor's Fermi level aligns with the redox potential of the electrolyte solution in the PEC cell, band bending takes place and an electric field is generated. This field facilitates the movement of photogenerated charges towards the semiconductor-electrolyte interface. For an n-type semiconductor photoanode, water can oxidize to oxygen.

Linear sweep voltammetry (LSV) with the illuminated pristine and Au_xCu_{1-x} NC-modified TNT electrodes (Figure 7a) shows, except for pure Au NCs, an increasing photocurrent density with increasing applied potential. The photocurrent density of the Au/TNTs increases up to 0.6 V versus the reversible hydrogen electrode (RHE) and stabilizes above this value. The pristine TNT electrode shows a linear trend up to 0.3 V_{RHE}, followed by a plateau in photocurrent density until 1.2 V_{RHE}, after which the current increases again. Under illumination TNTs and Au_xCu_{1-x}/TNTs electrodes can produce photogenerated electron-hole pairs, whose holes oxidize the water molecules at the anode and electrons reduce protons into molecular hydrogen at the cathode. As summarized in Figure 7c, the photocurrent density at 1.23 V_{RHE} is strongly enhanced by the presence of the NCs. In particular, the photoanode with $Au_{0.25}Cu_{0.75}$ NCs produces 244 μA/cm^2 at 1.23 V_{RHE}, which is 3.5 times higher than the corresponding value (68 μA/cm^2) for pristine TNTs. This $Au_{0.25}Cu_{0.75}$/TNT result is significantly higher than the values reported (150 μA/cm^2 and 64 μA/cm^2) in the literature for PEC application using AuCu nanoparticles on TNTs.[43,44] The photoresponse of the electrodes under chopped illumination (switching the light source on and off every 5 seconds) when performing LSV is presented in Figure 7b. It gives an indication of current under both light and dark conditions exhibited by photoanodes. The current density at a bias of 1.23 V_{RHE} without light is also included in Figure 7c as a reference for the photocurrent. The dark current probably arises from the electrocatalytic performance of Cu_2O. A detailed discussion of the electrocatalytic nature of Cu_2O is beyond the scope of this work.

View Article Online
DOI: 10.1039/D4NR03219E

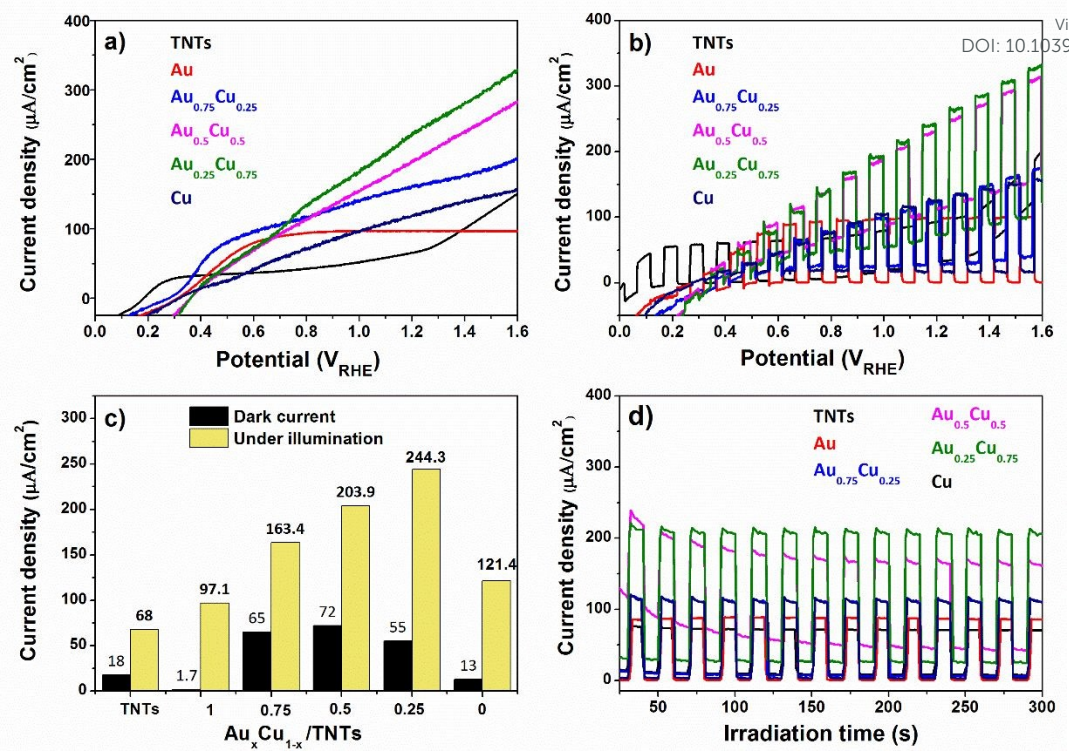

Figure 7. a) LSV of the pristine and Au_xCu_{1-x} NC-modified TNT samples under AM 1.5G illumination; b) LSV under chopped illumination; c) Current density of the different photoanodes at 1.23 V_{RHE}, without light and under illumination; d) Chronoamperometry under chopped illumination at 1.23 V_{RHE}.

Chronoamperometric measurements at 1.23 V_{RHE} (Figure 7d) show a steady photocurrent for all electrodes and confirm the photocurrent enhancement upon NC modification, particularly with bimetallic Au_xCu_{1-x} NCs. The $Au_{0.25}Cu_{0.75}$ modified TNTs photoanode performs the best. It was found to be photostable at 1.23 V_{RHE} for at least 1 hour (see supplementary information Figure S5). The small activity drop observed at the beginning of the measurements can be related to the re-oxidation of a fraction of copper in the first seconds (see assessment of the possible current generated by the oxidation of copper in the supplementary information), because the photoanodes were reduced before PEC testing. After a period of 90 days, this electrode retained 90% from its initial activity confirming its resistance to ambient conditions.

The applied bias to photon conversion efficiency (ABPE), as calculated using equation (1) discussed in section 5.3 from values obtained by LSV under illumination, is depicted in Figures 8a and 8b. The pristine TNTs electrode exhibits the lowest ABPE of 0.023 at 0.6 V_{RHE}, while $Au_{0.75}Cu_{0.25}$/TNTs demonstrates a maximum ABPE of 0.061% at 0.6 V_{RHE}. The $Au_{0.25}Cu_{0.75}$/TNTs sample which has the highest photocurrent at 1.23 V_{RHE}, shows a slightly lower ABPE of 0.044 % at 0.6 V_{RHE}.

The interfacial charge transfer efficiency of the photoelectrodes at their interface with the electrolyte was evaluated using electrochemical impedance spectroscopy (EIS) measured in 0.5 M Na_2SO_4 electrolyte at pH 7.2 under AM 1.5G illumination. The Nyquist plot in Figure 8c shows that $Au_{0.25}Cu_{0.75}$-modified TNTs exhibits the smallest circle arc followed successively by $Au_{0.5}Cu_{0.5}$, $Au_{0.75}Cu_{0.25}$, Cu, and Au NC-modified TNTs, while the pristine TNTs sample exhibits the largest arc. The smaller arc radii in AuCu/TNTs electrodes indicates good electrode-electrolyte interfacial charge transfer with lower charge transfer resistance as compared with pristine TNTs.

The hole relaxation lifetime can be calculated through the Bode phase analysis presented in Figure 8d. An accelerated lifetime and a minimal hole diffusion length are key factors for a rapid charge transfer process at the interface, resulting in an improved water oxidation performance. Using equation (2) the hole-relaxation time for $Au_{0.25}Cu_{0.75}$/TNTs is 40 ms, which is substantially shorter than the corresponding lifetime of bare TNTs of 160 ms. This results, using equation (3), in a shorter hole diffusion length for $Au_{0.25}Cu_{0.75}$/TNTs (0.45 mm) than in the bare TNTs (0.91 mm). The dark current densities cannot be ignored since all bimetallic AuCu/TNTs electrodes exhibit a nonzero dark current as seen in LSV under chopped illumination (Figure 7b and 7c), originating from the electrocatalytic performance of AuCu in oxidative reactions.[76-80] The total current generated by the copper containing electrodes is a combination of electrocatalytic and photocatalytic reactions facilitating a synergistic interaction between the photons and electricity. This synergy contributes to achieving optimal PEC performance.

View Article Online
DOI: 10.1039/D4NR03219E

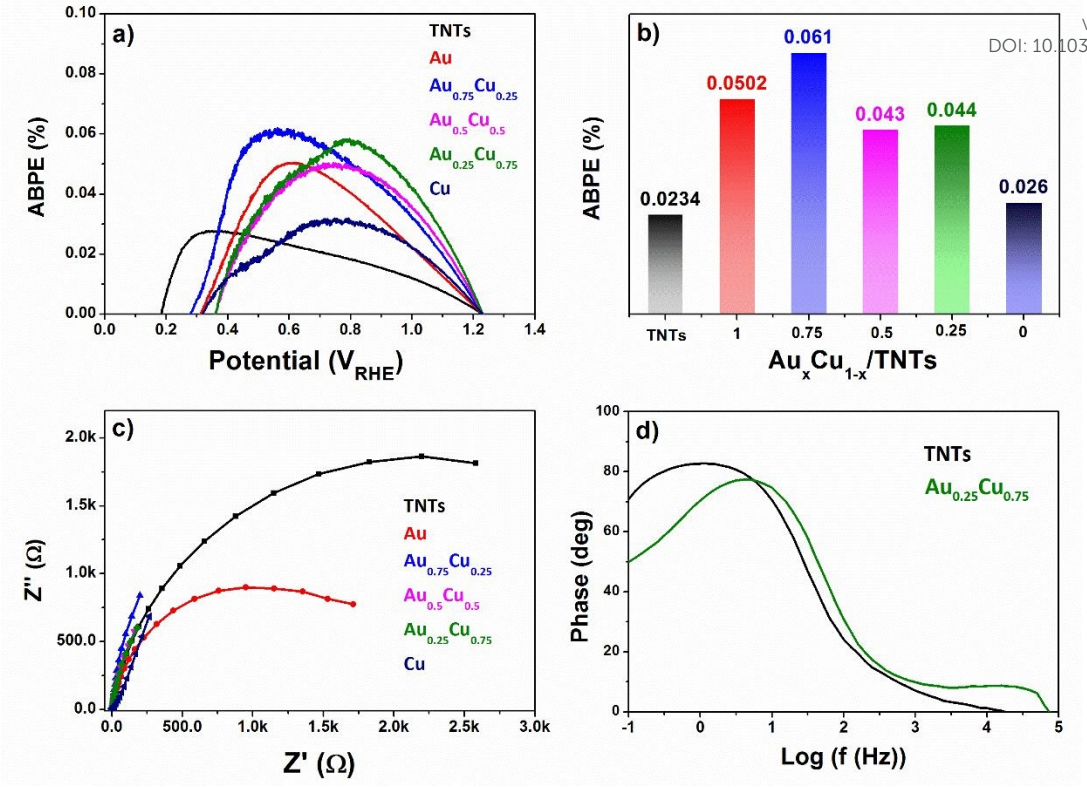

Figure 8. a) ABPE plot of all electrodes; b) ABPE values at 0.6 V_{RHE}; c) EIS spectra of pristine and $AuCu_{1-x}$ /TNT (x= 1, 0.75, 0.5, 0.25 and 0) electrodes measured under AM 1.5G illumination d) Bode plot of pristine TNT and $Au_{0.25}Cu_{0.75}$ / TNT, measured in 0.5 M Na_2SO_4 at pH 7.2.

3. Discussion

CBD technology enabled the production of NCs/TNTs with an optimal 4 ML metal loading which allows the TNTs photocatalyst to harvest sunlight effectively and generate more charge carriers, while samples with higher loading of 6 ML and 8 ML exhibit a lower photocurrent density (see supplementary information Figure S6). At those higher loadings, the direct exposure of the TNT to the light gradually gets blocked. A similar loading dependence was found in earlier work on the photocatalytic stearic acid degradation using titania nanoparticles decorated with pure gold and alloy AuAg NCs.[40,81]

Electrodes modified by Au_xCu_{1-x} NCs present composition-dependent atomic arrangements that exhibit very distinctive PEC activity suggesting a direct composition-to-PEC performance relationship. We cannot exclude that small differences in the NC sizes of the different Au_xCu_{1-x} NC modified electrodes have an influence on the PEC activity as well, but we expect this influence to be limited since the main contribution of the NCs on the PEC activity is through their plasmonic effect and the plasmonic properties of the NCs vary only slightly with size in the size range of a few nanometers.[82] Monometallic Au and Cu cluster-modified electrodes exhibit a relatively limited photocurrent enhancement compared to the pristine TNTs. The 40% enhanced PEC activity of Au NCs/TNT compared to pristine TNTs likely originates from the strong plasmonic properties of the metallic gold clusters, as well as from their low charge carrier recombination, highlighted by the low PL emission intensity. This is supported by the very low dark current of this electrode. The Au/TNT electrode suffers however from a high charge transfer resistance at the electrode-electrolyte interface as observed by EIS measurements that may limit the PEC activity enhancement. On the other hand, the Cu NCs, consisting of a small core of Cu metal surrounded by Cu_2O and CuO on the surface, feature a remarkable 80% increase in PEC activity compared to pristine TNTs at 1.23 V_{RHE}. The small dark current of 13 μA/cm^2 can originate from the 2 eV band gap of the 33% Cu_2O oxide layer, while 89% of activity (108 μA/cm^2) is triggered by light. The improvement of the photogenerated charge carrier separation, reflected in the limited attenuation of the PL, as well as its poor stability, may limit the PEC performance of the monometallic Cu/TNT electrode.

All bimetallic Au_xCu_{1-x} NCs/TNTs electrodes deliver higher photocurrent densities than the monometallic ones. Upon alloying gold with copper, the current density increases by 68%, 91%, and 152% for x = 0.75, 0.5, and 0.25, respectively, compared to that of Au NCs/TNT. This composition-dependent PEC activity, peaking at $Au_{0.25}Cu_{0.75}$, can be attributed to a synergy between both metals,[82,83] possibly in the form of the Au-CuO heterostructures observed by STEM-EDS at the surface of the NPs that consist of two complementary active sites as highlighted previously under CO oxidation where CO adsorbed on Au reacts with a contiguous labile CuO oxygen.[77] This synergy is further illustrated by the higher stability of the bimetallic NCs especially $Au_{0.25}Cu_{0.75}$/TNTs and by the composition-dependent quenching of the PL, which is stronger for higher copper content in the alloy.

Au-rich $Au_{0.75}Cu_{0.25}$/TNTs demonstrates the highest ABPE at 0.6 V_{RHE} and shows a 68 % photocurrent increase at 1.23 6 V_{RHE} compared to pure Au NCs. On the other hand, $Au_{0.75}Cu_{0.25}$/TNT shows a higher recombination of charge carriers compared to its pure Au counterpart as observed by its higher PL intensity but lower charge transfer resistance. It exhibits a dark current of 65 μA/cm^2, and

98 μA/cm² under light exposure (Figure 7c) at 1.23 V_{RHE}. As the structural arrangement of $Au_{0.75}Cu_{0.25}$ NCs consists of a large pure gold or gold-rich metallic core (around 85%) surrounded by a thin Cu_2O / CuO layer at the surface, it features a higher plasmon intensity than the other alloy electrodes. As $Au_{0.75}Cu_{0.25}$ differs mostly from pure Au by the presence of a thin CuO_x layer, this copper oxide may be responsible for its higher activity.

$Au_{0.5}Cu_{0.5}$/TNTs demonstrates a 25% increase in activity compared to $Au_{0.75}Cu_{0.25}$ at 1.23 V_{RHE}. On the other hand, it shows lower recombination of charge carriers and charge transfer resistances as observed by its lower PL intensity and EIS, respectively. $Au_{0.5}Cu_{0.5}$ NCs consist of a pure gold / gold-rich random alloy at the core (56%). They differ from $Au_{0.75}Cu_{0.25}$ NCs by their smaller metallic core and thicker CuO_x (36%) surface layer. This structural arrangement is expected to further reduce the plasmon intensity, while the higher amount of copper oxide at the surface may be at the origin of its higher activity. The discrepancy between XPS and XAFS measurements indicate that NCs with this composition are unstable and their actual *in situ* structural arrangement may thus be different from the one presented in Figure 5.

Finally, the copper-rich $Au_{0.25}Cu_{0.75}$/TNT exhibits the highest PEC activity of all tested electrodes. The main structural difference with $Au_{0.5}Cu_{0.5}$ lies in the presence of an intermetallic $Au_{0.5}Cu_{0.5}$ alloyed structure with small amount (58%) of pure Cu metal in the core. As similar amounts of copper oxide are positioned at the surface of the metallic cores in $Au_{0.25}Cu_{0.75}$ and $Au_{0.5}Cu_{0.5}$ NCs, the presence on an intermetallic alloy may be at the origin of the activity increase of $Au_{0.25}Cu_{0.75}$/TNT.

All bimetallic Au_xCu_{1-x} NCs have core/shell structures in the ambient, resulting from the segregation and oxidation of copper at the surface of the NC leading. Similar core/shell structures have been reported for AuCu nanoalloys under oxidative conditions.[83] This phase segregation leads to the formation of surface CuO_x that boosts the CO oxidation catalytic activity,[77-80,86] due to a bifunctional mechanism where CO activation takes place on Au atoms, while the O_2 species are activated on Cu rich sites.[10] A similar mechanism is supported by the present study where we find a significant activity of bimetallic NCs in the absence of light (65 to 72 μA/cm²), opposed to the negligible activity of their monometallic counterparts. The segregation process depends on the composition and structure of the AuCu alloys as fcc-AuCu and fct-AuCu nanoparticles tend to transform into different Au/CuO and AuCu/CuO core/shell structures, due to distinct Cu diffusion properties, that in turn confer them distinct catalytic activities.[77]

The bimetallic Au_xCu_{1-x} NCs/TNTs electrodes all present reduced recombination of charge carriers, as indicated by the low PL intensity, implying the generated charge carriers are efficiently separated by the NCs, which act as electron sinks. They also demonstrate a good interfacial charge transfer efficiency as evidenced by the EIS results. Beside the photophysical activity of the Cu_2O oxide layer at their surface, all bimetallic Au_xCu_{1-x} NCs feature a large plasmonic metallic core accounting for 56 to 85% of the cluster atoms that will resonate under visible light illumination. The resulting hot carriers have longer relaxation times and mean free paths and thus become efficient LSPR materials as shown in literature.[87,88] The distinct electronic properties of the fct-AuCu intermetallic alloys may also contribute to the higher activity of $Au_{0.25}Cu_{0.75}$ as the crystallographic ordering of atoms is indeed expected to significantly affect the band structure of the NPs as this one depends critically on the directional overlap of atomic orbitals.[77] Intermetallic compounds show larger hot carrier generation, originating mainly from direct interband and phonon-assisted indirect electronic transitions.[87] The resulting hot carriers are energetically higher than those in their monometallic counterparts, which may explain the highest photoactivity of $Au_{0.25}Cu_{0.75}$, featuring an intermetallic core. The improved stability in time of the intermetallic structure in $Au_{0.25}Cu_{0.75}$ NCs that unlike the $Au_{0.5}Cu_{0.5}$ counterparts do not segregate after a few days in the ambient as well as under reaction conditions may also explain their higher activity. Hence, the highest activity of $Au_{0.25}Cu_{0.75}$ results from a combination of factors highlighting the complex and tunable structure-activity relationship in these photocatalysts.

4. Conclusion

In summary, dispersed ligand-free Au_xCu_{1-x} (x = 1, 0.75, 0.5, 0.25 and 0) NCs were grown and deposited, by the CBD method, on TNTs. It was observed that surface modification of TNTs with Au_xCu_{1-x} NCs leads to enhanced PEC activity under solar irradiation peaking for the $Au_{0.25}Cu_{0.75}$ NC composition, which shows a four-fold enhancement in photocurrent compared to pristine TNTs. Reduced recombination of charge carriers as indicated by the lowest PL intensity, and the highest interfacial charge transfer efficiency as evidenced by the impedance spectroscopy, contribute to the superior performance of this electrode. The enhancement is attributed to a synergy between Au and Cu in the NCs that upon segregation produces bifunctional sites consisting of metallic Au/AuCu alloy and surface copper oxide, whose activity is boosted mostly by the photophysical plasmonic response of the metal under solar light illumination. The distinct ftc-AuCu ordered structure of the alloy, present in the most active $Au_{0.25}Cu_{0.75}$ NCs, may also contribute to the activity as it may improve the NC stability and the photophysical and chemical catalytic performance. Finally, this work highlights the potential of the CBD technique that produces ligand-free NCs of tuneable size and composition with a high degree of purity and high uniformity, which serves as an ideal technology to investigate cluster properties and at the same time to design efficient cluster-based photocatalysts for PEC water oxidation.

5. Experimental section

5.1. Preparation of AuCu NCs modified samples

A one-step anodization process was used to convert metallic titanium in a porous titanium oxide film with controllable pore size and good uniformity.[89] The Ti foil (1 mm thick, 1 × 1 cm²) was first ultrasonically cleaned and rinsed with acetone, ethanol, distilled water, and then dried under N_2 gas flow for a few seconds and finally anodized for 2 h in an electrolyte mixture containing 40 ml of ethylene glycol, 0.5 wt% of ammonium fluoride, and 2 vol% water. A platinum foil (1 × 1 cm²) was used as the cathode and a 30 V DC voltage was applied (Voltcraft PPS DC power supply). The grown TNTs were cleaned with distilled water and dried under a N_2 stream. Subsequently, the samples were subjected to a 2 h heat treatment at 450 °C, aiming to transform the amorphous regions of the nanotube walls into the titania anatase phase.[90,91] This step reduces

the presence of charge carrier recombination centers. Next, the prepared TNT substrates were modified with AuCu NCs with equivalent atomic coverages of 4 ML.

The NCs are produced by pulsed laser (10 Hz, Nd:YAG laser, INDI, Spectra Physics) ablation of mono and bimetallic Au_xCu_{1-x} (x = 1, 0.75, 0.5, 0.25 and 0) plate targets (ACI Alloy, purity 99.995%) and condensation in a helium atmosphere (introduced though a pulsed valve with a backing pressure of 7 bar). Following expansion into vacuum a beam of clusters is formed. The cluster size distribution can be tuned by adjusting the laser energy density, the helium pressure, and the time lag between the target ablation and the introduction of the He carrier gas.[48,92,93] The AuCu NCs are deposited on the TNTs supports by simply placing the supports perpendicular to the molecular beam in a high vacuum deposition chamber (6.8×10^{-8} h Pa). The deposition occurs under soft-landing conditions, given a speed of the cluster beam of about 700 m s^{-1} (corresponding to a kinetic energy of 0.3 eV per atom).

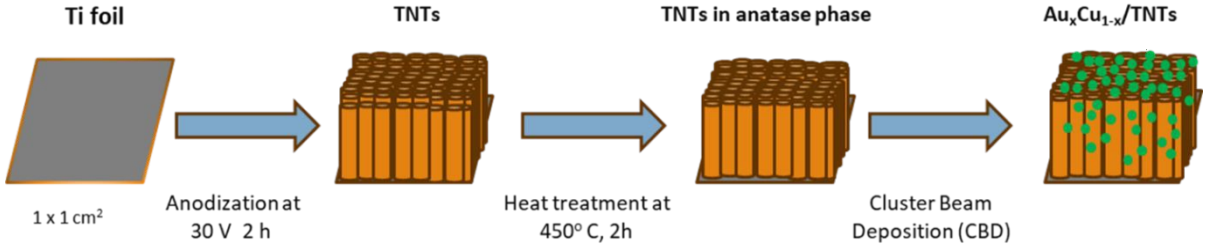

Figure 9: Schematic illustration summarizing the synthesis of TNTs from a titanium foil and the subsequent deposition of Au_xCu_{1-x} NCs.

5.2. Characterization

Different characterization techniques were applied to investigate the structural (X-ray diffraction, electron microscopy), optical (UV-Vis and photoluminescence), and photoelectrochemical properties of the TNTs modified with the Au_xCu_{1-x} NCs.

XRD was performed on all Au_xCu_{1-x} NC-modified TNT samples using a Bruker D8 advance diffractometer equipped with a LYNXEYE XE-T detector and Cu Kα source emitting radiation of 1.54 Å. Measurements spanned a 2θ range from 10° to 90°, with a scan rate of 0.5 s $step^{-1}$. The diffractograms were analyzed using Bruker's DIFFRAC.EVA software, with phase identification achieved by comparison with the ICDD database.

The surface morphology of the as-prepared samples was characterized with SEM using a FEI Helios Nanolab G3 CX system (acceleration voltage of 10 kV). The cluster size distributions and compositions were analyzed with Transmission Electron Microscopy (TEM) using an aberration corrected Thermo Fischer Scientific Titan instrument. For the TEM studies, the Au_xCu_{1-x} NCs were deposited on molybdenum grids. The TEM was used at an accelerating voltage of 120 kV. Particle size distributions were obtained via the 'ImageJ' image analysis software.

Ultraviolet-Visible light absorbance spectra (UV-Vis) of cluster decorated TNTs samples were obtained in the 300-700 nm wavelength range using a double beam UV 2600 photospectrometer (Shimadzu, Kyoto, Japan) equipped with film holders attached to a $BaSO_4$ coated integrating sphere of 60 mm in diameter. Steady state photoluminescence (PL) spectra were measured at room temperature using Shimadzu RF-6000 fluorescence spectro-photometer equipped with a 150 W xenon lamp and a 1 nm resolution of the measured emission spectra. All PL measurements were performed at an excitation wavelength of 310 nm.

XPS measurements were performed at room temperature using a laboratory setup equipped with a Mg KαX-ray and an Alpha 110 hemispherical Analyzer.

EXAFS and XANES experiments were performed at the LISA beamline (BM08)[94] of the European Synchrotron Radiation Facility (ESRF, Grenoble, France), operating in a 7/8 multi bunch mode with a current of 200 mA. Data was collected at the Au L_3-edge (E = 11919 eV) and the Cu K-edge (E = 8979 eV) in grazing incidence (incidence angle ~ 2° with the beam polarization perpendicular to the surface) and using fluorescence detection mode.

5.3. Photoelectrochemical applications

The photoelectrochemical performance of the pristine and AuCu alloy NC-modified TNTs was studied using a three-electrode configuration in 0.5 M Na_2SO_4 at pH = 7.21. The pristine and NC modified electrodes (1 × 1 cm^2), platinum foil and aqueous silver/silver chloride (Ag/AgCl) electrodes were used as a working, counter, and reference electrodes, respectively. The performance of each working electrode was evaluated using LSV, chronoamperometry, and EIS. EIS of prepared photoanodes was measured, in the dark and under illumination, by applying an AC voltage amplitude of 10 mV at open circuit potentials (OCV) with a frequency ranging from 100 mHz to 100 kHz. All measured potentials were converted to reversible hydrogen electrode (RHE) scale using the Nernst equation.

The Scisun-300 solar simulator from Sciencetech, equipped with a xenon arc lamp and AM 1.5G filter, was used as a light source. The intensity of the light source was adjusted to 100 mW/cm^2 by changing the working distance and was measured using an Avantes photospectrometer. To check and screen the PEC performance, the prepared electrodes were tested in a single PEC cell and the electrodes were positioned as close as possible to the front of quartz window to minimize the influence of light absorption by water.

The *ABPE* was calculated from the LSV data.

$$ABPE = \frac{J_{ph}(\text{mA cm}^{-2}) \times (1.23 - V)(\text{V})}{P_{total}(\text{mW cm}^{-2})} \quad (1)$$

Where J_{ph} is the photocurrent obtained under applied potential V and P_{total} is the intensity of the light source. The charge transfer at the interface between the electrode and the electrolyte was studied through Bode phase analysis. The hole-relaxation time or electron lifetime τ and the hole diffusion length L_d are given by:

$$\tau = \frac{1}{2\pi f_{max}} \quad (2)$$

$$L_d = \sqrt{D\tau} \quad (3)$$

with f_{max} the frequency corresponding to the maximum phase in the range of 10 to 100 Hz and D is hole diffusion coefficient = 5×10^{-2} cm^2 s^{-1}.[95,96]

Author Contributions

V.C.C.: Conceptualization, investigation, formal analysis, visualization, writing original draft, editing; K.R.A.: Investigation, formal analysis; T.H.T.N, Z.Z, I.A., T.H.H.: Investigation; P.L.: supervision, editing, funding acquisition; D.G., S.V. & E.J.: Resources, supervision, writing, editing, validation, funding acquisition.

Conflicts of interest

There are no conflicts to declare.

Data availability

The raw data that was used for the figures included in the manuscript and the supplementary information is available on KU Leuven's institutional research data repository at https://rdr.kuleuven.be/dataverse/rdr doi 10.48804/0UXAXQ.

Acknowledgements

This research work has been supported by Flanders Innovation & Entrepreneurship (VLAIO) under project No. HBC.2021.0586 (CLUE). V.C.C. is supported by the Jesuit region of the European Low Countries (ELC). T.H.T. Nguyen thanks the Research Foundation Flanders (FWO) for an FWO MSCA SoE postdoctoral fellowship (12ZZI.23N). E.J. acknowledges FWO for a sabbatical bench fee (K800124N). The authors thank Thomas Altantzis and Sara Bals (EMAT, University of Antwerp) for providing the HAADF-STEM and EDX data of the $Au_{0.25}Cu_{0.75}$ clusters. They also thank the ESRF for providing beamtime (HC-5047) and the staff of LISA-BM08 for their assistance.

References

1 R. K. Keswani, H. Ghodke, D. Sarkar, K. C. Khilar and R. S. Srinivasa, *Colloids Surf. Physicochem. Eng. Asp.*, 2010, **369**, 75–81.
2 B. Liu, D. Deng, J. Y. Lee and E. S. Aydil, *J. Mater. Res.*, 2010, **25**, 1588–1594.
3 Z. Zander, R. Yagloski, J. DeCoste, D. Zhang and B. G. DeLacy, *Mater. Lett.*, 2016, **163**, 39–42.
4 J. M. Macak, H. Hildebrand, U. Marten-Jahns and P. Schmuki, *J. Electroanal. Chem.*, 2008, **621**, 254–266.
5 G. D. Sulka, J. Kapusta-Kołodziej, A. Brzózka and M. Jaskuła, *Electrochimica Acta*, 2010, **55**, 4359–4367.
6 J. M. Macak, H. Tsuchiya, A. Ghicov, K. Yasuda, R. Hahn, S. Bauer and P. Schmuki, *Curr. Opin. Solid State Mater. Sci.*, 2007, **11**, 3–18.
7 G. D. Sulka, J. Kapusta-Kołodziej, A. Brzózka and M. Jaskuła, *Electrochimica Acta*, 2013, **104**, 526–535.
8 J. M. Macak and P. Schmuki, *Electrochimica Acta*, 2006, **52**, 1258.
9 S. Bauer, S. Kleber and P. Schmuki, *Electrochem. Commun.*, 2006, **8**, 1321–1325.
10 V. Zwilling, M. Aucouturier and E. Darque-Ceretti, *Electrochimica Acta*, 1999, **45**, 921–929.
11 D. Gong, C. A. Grimes, O. K. Varghese, W. Hu, R. S. Singh, Z. Chen and E. C. Dickey, *J. Mater. Res.*, 2001, **16**, 3331–3334.
12 H. Brahmi, G. Katwal, M. Khodadadi, S. Chen, M. Paulose, O. K. Varghese and A. Mavrokefalos, *Nanoscale*, 2015, **7**, 19004–19011.
13 X. Chen and S. S. Mao, *Chem. Rev.*, 2007, **107**, 2891–2959.
14 S. Shen, J. Chen, M. Wang, X. Sheng, X. Chen, X. Feng and S. S. Mao, *Prog. Mater. Sci.*, 2018, **98**, 299–385.
15 M. Ge, Q. Li, C. Cao, J. Huang, S. Li, S. Zhang, Z. Chen, K. Zhang, S. S. Al-Deyab and Y. Lai, *Adv. Sci.*, 2017, **4**, 1600152
16 J. F. De Brito, F. Tavella, C. Genovese, C. Ampelli, M. V. B. Zanoni, G. Centi and S. Perathoner, *Appl. Catal. B Environ.*, 2018, **224**, 136–145.
17 M. Paulose, K. Shankar, S. Yoriya, H. E. Prakasam, O. K. Varghese, G. K. Mor, T. J. LaTempa, A. Fitzgerald and C. A. Grimes, *J. Phys. Chem. B*, 2006, **110**, 16179–16184.
18 J. M. Macak, M. Zlamal, J. Krysa and P. Schmuki, *Small Weinh. Bergstr. Ger.*, 2007, **3**, 300–304.
19 Y. Jiang, B. Zheng, J. Du, G. Liu, Y. Guo and D. Xiao, *Talanta*, 2013, **112**, 129–135.
20 L. Martínez, L. Soler, I. Angurell and J. Llorca, *Appl. Catal. B Environ.*, 2019, **248**, 504–514.
21 S. Abela, C. Farrugia, R. Xuereb, F. Lia, E. Zammit, A. Rizzo, P. Refalo and M. Grech, *Nanomaterials*, 2021, **11**, 2823.
22 S. Asadi, B. Mortezagholi, A. Hadizadeh, V. Borisov, M. J. Ansari, H. Shaker Majdi, A. Nishonova, H. Adelnia, B. Farasati Far and C. Chaiyasut, *Pharmaceutics*, 2022, **14**, 1359.
23 M. Yamaguchi, H. Abe, T. Ma, D. Tadaki, A. Hirano-Iwata, H. Kanetaka, Y. Watanabe and M. Niwano, *Langmuir*, 2020, **36**, 12668–12677.
24 K. Shankar, J. I. Basham, N. K. Allam, O. K. Varghese, G. K. Mor, X. Feng, M. Paulose, J. A. Seabold, K.-S. Choi and C. A. Grimes, *J. Phys. Chem. C*, 2009, **113**, 6327–6359.
25 P. Szymanski and M. A. El-Sayed, *Theor. Chem. Acc.*, 2012, **131**, 1202.
26 S. A. Batool, M. Salman Maqbool, M. A. Javed, A. Niaz and M. A. U. Rehman, *Surfaces*, 2022, **5**, 456–480.
27 M. Grätzel, *Nature*, 2001, **414**, 338–344.
28 S. U. M. Khan, M. Al-Shahry and W. B. Ingler, *Science*, 2002, **297**, 2243–2245.
29 M. R. Khan, T. W. Chuan, A. Yousuf, M. N. K. Chowdhury and C. K. Cheng, *Catal. Sci. Technol.*, 2015, **5**, 2522–2531.
30 S. Linic, P. Christopher and D. B. Ingram, *Nat. Mater.*, 2011, **10**, 911–921.
31 M. G. Méndez-Medrano, E. Kowalska, A. Lehoux, A. Herissan, B. Ohtani, D. Bahena, V. Briois, C. Colbeau-Justin, J. L. Rodríguez-López and H. Remita, *J. Phys. Chem. C*, 2016, **120**, 5143–5154.
32 Z. Hai, N. E. Kolli, D. B. Uribe, P. Beaunier, M. José-Yacaman, J. Vigneron, A. Etcheberry, S. Sorgues, C. Colbeau-Justin, J. Chen and H. Remita, *J. Mater. Chem. A*, 2013, **1**, 10829–10835.
33 P. A. Gross, S. N. Pronkin, T. Cottineau, N. Keller, V. Keller and E. R. Savinova, *Catal. Today*, 2012, **189**, 93–100.

34 I. Paramasivam, J. M. Macak and P. Schmuki, *Electrochem. Commun.*, 2008, **10**, 71–75.
35 S. Zhang, F. Peng, H. Wang, H. Yu, S. Zhang, J. Yang and H. Zhao, *Catal. Commun.*, 2011, **12**, 689–693.
36 K. Xie, L. Sun, C. Wang, Y. Lai, M. Wang, H. Chen and C. Lin, *Electrochimica Acta*, 2010, **55**, 7211–7218.
37 Y. Wang, Z. Li, Y. Tian, W. Zhao, X. Liu and J. Yang, *Mater. Lett.*, 2014, **122**, 248–251.
38 K. Syrek, J. Grudzień, A. Sennik-Kubiec, A. Brudzisz and G. D. Sulka, *J. Nanomater.*, 2019, **2019**, e9208734.
39 R. Ferrando, J. Jellinek and R. L. Johnston, *Chem. Rev.*, 2008, **108**, 845–910.
40 V. C. Chinnabathini, F. Dingenen, R. Borah, I. Abbas, J. van der Tol, Z. Zarkua, F. D'Acapito, T. H. T. Nguyen, P. Lievens, D. Grandjean, S. W. Verbruggen and E. Janssens, *Nanoscale*, 2023, **15**, 6696–6708.
41 B. Zhu, L.-Y. Zhang, J.-L. Liu, X.-M. Zhang, X.-S. Li and A.-M. Zhu, *J. Hazard. Mater.*, 2021, **402**, 123508.
42 Ş. Neaţu, J. A. Maciá-Agulló, P. Concepción and H. Garcia, *J. Am. Chem. Soc.*, 2014, **136**, 15969–15976.
43 Z.-Y. Li, Y.-H. Chen, J.-R. Zhu, Q. Chen, S.-J. Lu and F.-X. Xiao, *Inorg. Chem.*, 2023, **62**, 16965–16973.
44 W. Lipińska, K. Grochowska, J. Ryl, J. Karczewski and K. Siuzdak, *ACS Appl. Mater. Interfaces*, 2021, **13**, 52967–52977.
45 M. Nischk, P. Mazierski, Z. Wei, K. Siuzdak, N. A. Kouame, E. Kowalska, H. Remita and A. Zaleska-Medynska, *Appl. Surf. Sci.*, 2016, **387**, 89–102.
46 Q.-L. Mo, X.-C. Dai and F.-X. Xiao, *Small*, 2023, **19**, 2302372.
47 Y. Pang, G. Xu, Q. Feng, J. Lv, Y. Qin, Y. Zhang, Z. Zheng and Y. Wu, *Phys. Lett. A*, 2018, **382**, 2759–2762.
48 B. Pauwels, G. Van Tendeloo, E. Zhurkin, M. Hou, G. Verschoren, L. Theil Kuhn, W. Bouwen and P. Lievens, *Phys. Rev. B*, 2001, **63**, 165406.
49 P. Milani and S. Iannotta, *Cluster Beam Synthesis of Nanostructured Materials*, Springer Science & Business Media, 2012.
50 R. Liu, Q. Li and L. M. Smith, *J. Am. Soc. Mass Spectrom.*, 2014, **25**, 1374–1383.
51 D. Hong, A. Sharma, D. Jiang, E. Stellino, T. Ishiyama, P. Postorino, E. Placidi, Y. Kon and K. Koga, *ACS Omega*, 2022, **7**, 31260–31270.
52 T. K. Sham, Y. M. Yiu, M. Kuhn and K. H. Tan, *Phys. Rev. B*, 1990, **41**, 11881–11886.
53 R. E. Watson, J. Hudis and M. L. Perlman, *Phys. Rev. B*, 1971, **4**, 4139–4144.
54 W. Eberhardt, S. C. Wu, R. Garrett, D. Sondericker and F. Jona, *Phys. Rev. B*, 1985, **31**, 8285–8287.
55 T. K. Sham, M. L. Perlman and R. E. Watson, *Phys. Rev. B*, 1979, **19**, 539–545.
56 M. Kuhn and T. K. Sham, *Phys. Rev. B*, 1994, **49**, 1647–1661.
57 P. Weinberger, A. M. Boring, R. C. Albers and W. M. Temmerman, *Phys. Rev. B*, 1988, **38**, 5357–5362.
58 J. E. Müller, O. Jepsen and J. W. Wilkins, *Solid State Commun.*, 1982, **42**, 365–368.
59 T.-W. Liao, A. Yadav, K.-J. Hu, J. van der Tol, S. Cosentino, F. D'Acapito, R. E. Palmer, C. Lenardi, R. Ferrando, D. Grandjean and P. Lievens, *Nanoscale*, 2018, **10**, 6684–6694.
60 I. J. Godfrey, A. J. Dent, I. P. Parkin, S. Maenosono and G. Sankar, *J. Phys. Chem. C*, 2017, **121**, 1957–1963.
61 J. T. Miller, A. J. Kropf, Y. Zha, J. R. Regalbuto, L. Delannoy, C. Louis, E. Bus and J. A. van Bokhoven, *J. Catal.*, 2006, **240**, 222–234.
62 R. E. Benfield, D. Grandjean, M. Kröll, R. Pugin, T. Sawitowski and G. Schmid, *J. Phys. Chem. B*, 2001, **105**, 1961–1970.
63 A. Yadav, Y. Li, T.-W. Liao, K.-J. Hu, J. E. Scheerder, O. V. Safonova, T. Höltzl, E. Janssens, D. Grandjean and P. Lievens, *Small*, 2021, **17**, 2170139.
64 S. Zhao, Z. Cheng, S. Wang, H. Hao and Y. Fang, *Appl. Phys. A*, 2021, **127**, 930.
65 D. Albinsson, S. Nilsson, T. J. Antosiewicz, V. P. Zhdanov and C. Langhammer, *J. Phys. Chem. C*, 2019, **123**, 6284–6293.
66 Z. Guo, O. V. Prezhdo, T. Hou, X. Chen, S.-T. Lee and Y. Li, *J. Phys. Chem. Lett.*, 2014, **5**, 1642–1647.
67 S. Kurian, H. Seo and H. Jeon, *J. Phys. Chem. C*, 2013, **117**, 16811–16819.
68 F.-X. Xiao, S.-F. Hung, J. Miao, H.-Y. Wang, H. Yang and B. Liu, *Small*, 2015, **11**, 554–567.
69 M. Szkoda, K. Siuzdak, A. Lisowska-Oleksiak, J. Karczewski and J. Ryl, *Electrochem. Commun.*, 2015, **60**, 212–215.
70 Z. Zhang and P. Wang, *Energy Environ. Sci.*, 2012, **5**, 6506–6512.
71 Z. Zhang, L. Zhang, M. N. Hedhili, H. Zhang and P. Wang, *Nano Lett.*, 2013, **13**, 14–20.
72 T. H. Gfroerer, in *Encyclopedia of Analytical Chemistry*, John Wiley & Sons, Ltd, 2006.
73 B.-H. Lee, S. Park, M. Kim, A. K. Sinha, S. C. Lee, E. Jung, W. J. Chang, K.-S. Lee, J. H. Kim, S.-P. Cho, H. Kim, K. T. Nam and T. Hyeon, *Nat. Mater.*, 2019, **18**, 620–626.
74 T. Kiyonaga, M. Fujii, T. Akita, H. Kobayashi and H. Tada, *Phys. Chem. Chem. Phys.*, 2008, **10**, 6553–6561.
75 A. L. Linsebigler, G. Lu and J. T. Jr. Yates, *Chem. Rev.*, 1995, **95**, 735–758.
76 X. Liu, S. Cui, Z. Sun, Y. Ren, X. Zhang and P. Du, *J. Phys. Chem. C*, 2016, **120**, 831–840.
77 W. Zhan, J. Wang, H. Wang, J. Zhang, X. Liu, P. Zhang, M. Chi, Y. Guo, Y. Guo, G. Lu, S. Sun, S. Dai and H. Zhu, *J. Am. Chem. Soc.*, 2017, **139**, 8846–8854.
78 T. E. R. Fiuza and D. Zanchet, *ACS Appl. Nano Mater.*, 2020, **3**, 923–934.
79 Z. Xu, E. Lai, Y. Shao-Horn and K. Hamad-Schifferli, *Chem. Commun.*, 2012, **48**, 5626–5628.
80 Y. Yu, X. Dong, P. Chen, Q. Geng, H. Wang, J. Li, Y. Zhou and F. Dong, *ACS Nano*, 2021, **15**, 14453–14464.
81 T. W. Liao, S. W. Verbruggen, N. Claes, A. Yadav, D. Grandjean, S. Bals, P. Lievens, *Nanomaterials*, 2018, 8, 30
82 S. W. Verbruggen, M. Keulemans, J. A. Martens, S. Lenaerts, *J. Phys. Chem. C*, 2013, **117**, 19142-19145.
83 A. Shah, M. Akhtar, S. Aftab, A. H. Shah and H.-B. Kraatz, *Electrochimica Acta*, 2017, **241**, 281–290.
84 U. Latif-ur-Rahman, A. Shah, R. Qureshi, S. B. Khan, A. M. Asiri, A.-H. A. Shah, M. Ishaq, M. S. Khan, S. K. Lunsford and M. A. Zia, *Adv. Mater. Sci. Eng.*, 2015, **2015**, e638629.
85 T.-S. Kim, H. Choi, D. Kim, H. C. Song, Y. Oh, B. Jeong, J. Lee, K.-J. Kim, J. W. Shin, H. R. Byon, R. Ryoo, H. Y. Kim and J. Y. Park, *Appl. Catal. B Environ.*, 2023, **331**, 122704.
86 X. Liu, A. Wang, X. Wang, C.-Y. Mou and T. Zhang, *Chem. Commun.*, 2008, 3187.
87 C. Jian, J. Zhang, W. He and X. Ma, *Nano Energy*, 2021, **82**, 105763.
88 C. Jian, J. Zhang and X. Ma, *RSC Adv.*, 2020, **10**, 13277–13285.
89 D. Gong, C. A. Grimes, O. K. Varghese, W. Hu, R. S. Singh, Z. Chen and E. C. Dickey, *J. Mater. Res.*, 2001, **16**, 3331–3334.
90 Z. Hua, Z. Dai, X. Bai, Z. Ye, P. Wang, H. Gu and X. Huang, *Chem. Eng. J.*, 2016, **283**, 514–523.

View Article Online
DOI: 10.1039/D4NR03219E

91 K. Grochowska, N. Nedyalkov, J. Karczewski, Ł. Haryński, G. Śliwiński and K. Siuzdak, *Sci. Rep.*, 2020, **10**, 20506.
92 P. Ferrari, J. Vanbuel, Y. Li, T.-W. Liao, E. Janssens and P. Lievens, in *Gas-Phase Synthesis of Nanoparticles*, John Wiley & Sons, Ltd, 2017, pp. 59–78.
93 T. W. Liao, A. Yadav, P. Ferrari, Y. Niu, X. K. Wei, J. Vernieres, K. J. Hu, M. Heggen, R. E. Dunin-Borkowski, R. E. Palmer, K. Laasonen, D. Grandjean, E. Janssens, P. Lievens, *Chem. Mater.*, 2019, **31**, 10040-10048.
94 F. D'Acapito, G. Lepore, A. Puri, A. Laloni, F. Manna, E. Dettona, A. Luisa and A. Martin, *J. Synchrotron Radiat.*, 2019, **26**, 551-558.
95 G. Xing, N. Mathews, S. Sun, S. S. Lim, Y. M. Lam, M. Grätzel, S. Mhaisalkar and T. C. Sum, *Science*, 2013, **342**, 344–347.
96 S. D. Stranks, G. E. Eperon, G. Grancini, C. Menelaou, M. J. P. Alcocer, T. Leijtens, L. M. Herz, A. Petrozza and H. J. Snaith, *Science*, 2013, **342**, 341–344.

View Article Online
DOI: 10.1039/D4NR03219E

The data of this article are shown in the Figures and the Supplementary Information. The raw data behind these figures is available on KU Leuven's institutional research data repository at https://rdr.kuleuven.be/dataverse/rdr with doi 10.48804/0UXAXQ.